The Japan Society
of Applied Physics

PROGRESS REVIEW

Structural stability and electronic properties of 2D alkaline-earth metal silicides, germanides, and stannides

To cite this article: A. Y. Alekseev *et al* 2020 *Jpn. J. Appl. Phys.* **59** SF0801

View the article online for updates and enhancements.

Structural stability and electronic properties of 2D alkaline-earth metal silicides, germanides, and stannides

A. Y. Alekseev[1], D. B. Migas[1,2,3*], A. B. Filonov[1], V. E. Borisenko[1,2], and N. V. Skorodumova[4,5]

[1]*Belarusian State University of Informatics and Radioelectronics, P. Browka 6, 220013 Minsk, Belarus*
[2]*National Research Nuclear University MEPhI (Moscow Engineering Physics Institute), Kashirskoe shosse 31, 115409 Moscow, Russia*
[3]*Institute for Nuclear Problems of Belarusian State University, Bobruiskaya 11, 220006 Minsk, Belarus*
[4]*Multiscale Materials Modelling, Department of Materials and Engineering, Royal Institute of Technology (KTH), SE-10044 Stockholm, Sweden*
[5]*Department of Physics and Astronomy, Uppsala University, Box 516, SE-75121 Uppsala, Sweden*

[*]E-mail: migas@bsuir.by

We present the results of an extended theoretical study of the structure, phonon, electronic and optical properties of 2D alkaline-earth metal silicides, germanides and stannides (2D Me_2X, where Me=Mg, Ca, Sr, Ba and X=Si, Ge, Sn). The performed analysis has shown the occurrence of the pseudo passivation effect and ionic chemical bonding in these 2D Me_2X. In addition, the preformed investigation of their phonon spectra has shown the absence of imaginary frequencies indicating the stability of these 2D structures. The band structure calculations performed using the hybrid functional have revealed that all 2D Me_2X are semiconductors with the gap varying from 0.12 to 1.01 eV. Among them Mg- and Ca-based 2D materials are direct band-gap semiconductors with the first direct transition having appreciable oscillator strength. We also propose to consider ternary 2D silicides, germanides and stannides with different Me atoms as a feasible way to modify properties of parent 2D Me_2X.
© 2020 The Japan Society of Applied Physics

1. Introduction

Nanostructured materials have been in research focus for a long time due to their unusual and sometimes even amazing properties as compared to those of the parent bulk materials. It becomes possible as the properties of nanostructures are mostly defined by those of the surfaces, owing to the large surface-to-volume ratio, and by the influence of quantum confinement effects. Starting from graphene, now the other monolayer or 2D materials are considered as ready-to-use building blocks for many applications.[1–7] However, the reason why 2D materials (such as graphene, transition metal chalcogenides, boron nitride, …) can be stable and can be easily fabricated by exfoliation techniques is a weak van der Waals interaction between layers. In addition, the chemical vapor deposition and the other bottom-up methods are nowadays widely used to grow such 2D materials.[8–11] Very recently the formation of silicene, germanene and statene mainly on metallic substrates has been reported.[12–15] One double layer [three of them are necessary to build a unit cell for the ⟨111⟩-oriented slabs] represents the structure of these materials indicating a very large concentration of dangling bonds perpendicular to the surface due to the sp^3 hybridization contrary to the sp^2 hybridization in graphene where all bonds are in the graphene plane. Such dangling bonds in silicene, germanene and statene can be easily saturated by hydrogen or haloid atoms.[12–16] More information on fabrication, properties and applications of known 2D materials can be found in recent reviews.[1–16] However silicides have not been experimentally reported to exist as 2D materials.[16]

Silicides are known to be fully compatible with the common silicon technology and environmentally friendly materials.[17] In the 1D form they can sizably enhance the ability to fabricate various nanodevices.[18] A few years ago we suggested on the basis of results of ab initio calculations the possibility that the silicides of alkaline-earth metal of Mg, Ca, Sr and Ba (namely Mg_2Si, Ca_2Si, Sr_2Si and Ba_2Si) could be stable in the 2D form having the same structure as

transition metal chalcogenides.[19] Their stability was ascribed to the pseudo passivation effect of metal atoms and the ionic nature in the chemical bonding. Moreover, these 2D silicides were found to be semiconductors and some of them to have a direct band-gap.

Here, we report our recent results on the stability and electronic properties of the 2D germanides and stanides of Mg, Ca, Sr and Ba (we conventionally call them Me_2X, where Me=Mg, Ca, Sr, Ba and X=Si, Ge, Sn) in different structures (the T and Td phases) in comparison with corresponding 2D silicides. In addition, ternary compounds, which involve two different metal atoms, are considered as a feasible way to modify the properties of 2D binary materials.

2. Computational methods and details

The structural optimization of 2D Me_2X was performed by the first principles total energy projector-augmented wave method (code VASP)[20–23] with the screened hybrid functional of Heyd, Scuseria, and Ernzerhof (HSE).[24–28] The standard settings for the screening and Hartree–Fock mixing parameters were used. This functional allows for better description of the exchange-correlation interaction as compared to the common local density or generalized gradient approximation (GGA). 2D Me_2X were considered in a periodic arrangement of slabs separated by 12 Å of vacuum that was enough to assure negligible interaction between the slabs. All of the atoms in 2D structures were allowed to relax. The structural optimization was stopped when forces acting on the atoms were smaller than 0.01 eV Å^{-1}. Our calculations were performed with the cutoff energy of 360 eV. For the self-consistent procedure a 34 k-point mesh in the irreducible part of the Brillouin zone were used. The convergence of the total energy was better than 1 meV per formula unit. The charge distributions and transfers were analyzed utilizing the Bader method.[29]

To study phonon dispersion in 2D Me_2X, instead of HSE we used GGA within parametrization of Perdew–Burke–Ernzerhof (PBE)[30] for the exchange-correlation interaction since the HSE functional is very computationally demanding.

The finite-differences method was used for the calculation of harmonic force constants using $n \times n \times 1$ supercells and $6 \times 6 \times 1$ k-point mesh for structures in the T-phase and $4 \times 2 \times 1$ supercells and $3 \times 4 \times 1$ k-point mesh for structures in the Td-phase. The phonon properties were calculated using Phonopy package.[31] Although 2D structures under consideration exhibit the ionic nature of bonds,[19] the LO-TO splitting are not considered because it is absent in 2D structures.[32] For the self-consistent procedure we kept the same energy cutoff while the total energy and forces convergence criterions were sizably stringent (10^{-10} eV and 10^{-8} eV Å^{-1}, respectively) with respect to the case of the hybrid calculations.

The calculations of the band structures and dipole matrix elements (M) were carried out by means of the self-consistent full potential linearized augmented plane wave method in its scalar-relativistic version using WIEN2k package.[33] The structural parameters of 2D Me$_2$Si fully optimized by the projector-augmented wave method with HSE were used for these calculations. We applied the screened hybrid functional YS-PBE0 (which is similar to HSE).[34] We performed the self-consistent procedure on the grids of not less than 70 k-points in the irreducible part of the Brillouin zone. The dipole matrix elements were calculated for the first direct transition.

3. Structure and phonon properties of 2D Me$_2$X in the T phase

Even though the orthorhombic structure is the ground state for the Ca$_2$X, Sr$_2$X and Ba$_2$X bulks (the Pnma space group), in the case of very thin films (from the 2D to multilayer structures of ∼1.5 nm in thickness) the cubic structure, which is typical of the Mg$_2$X bulks (the anti-CaF$_2$ type structure, the Fm$\bar{3}$m space group), provides a sizable lowering in the surface energy and, as a result, in the total energy due to pseudo passivation effect.[19] The origin of this pseudo passivation effect is twofold. Firstly, it is the appearance of the Me atoms as top layers keeping the X atoms inside[19] (see Fig. 1). Secondly, the mostly ionic nature of the chemical

bonding in 2D Mg$_2$X (we will also show later in Sect. 5 that this is also true for 2D Ca$_2$X, Sr$_2$X and Ba$_2$X) "removes" surface dangling bonds by redistributing charge among the atoms in 2D Me$_2$Si.[19] Similar issues have already been observed for different BaSi$_2$ surfaces indicating that Ba atoms on the surface provided lower surface energy[35] and in different Ca$_2$Si nanostructures.[36]

Since the hexagonal symmetry is preserved for 2D Ca$_2$X, Sr$_2$X and Ba$_2$X (like in some transition metal dichalcogenides known to exist in the so called T phase[19]), each X atom has six Me atoms as first neighbors while for Me atoms only three X atoms can be counted as first neighbors. Details on 2D Ca$_2$X, Sr$_2$X and Ba$_2$X structures are summarized in Table I indicating some clear tendencies. Thus, the lattice parameter (a) substantially increases when moving from materials with different Me atoms but the same X atom, while very slight changes can be spotted in the rows of the same Me atoms and different X atoms (only stannides displayed larger a). As a consequence, the same trends are evident for interatomic (d_{Me-X}) and interplane (d_{ip}) distances. For example, in the row of Ca$_2$Si–Ca$_2$Ge–Ca$_2$Sn a varies as 4.72–4.74–5.07 Å to be compared to 4.75–4.96–5.12 Å for the row of Ca$_2$Ge–Sr$_2$Ge–Ba$_2$Ge. In the case of d_{Me-X} and d_{ip} one can trace the following: 2.96–2.98–3.15 Å versus 2.98–3.15–3.32 Å and 1.15–1.16–1.15 Å versus 1.16–1.32–1.51 Å, respectively for the same rows. It is also important to emphasize that the X atoms do not directly interact with each other because the X–X interatomic distances coincide with a, which is rather large (close to 5 Å).

The calculated phonon dispersions along with discussion on the dynamical stability of 2D Me$_2$X have been presented in our previous paper.[37] All calculated phonon dispersions contained imaginary frequencies in the acoustic out-of-plane phonon branch (the so-called ZA branch) in the vicinity of the Γ point. We have already clarified that these imaginary frequencies did not necessarily point to the dynamical instability and originated from inaccuracy of calculations due to the limited supercells size and, possibly, to a failure of
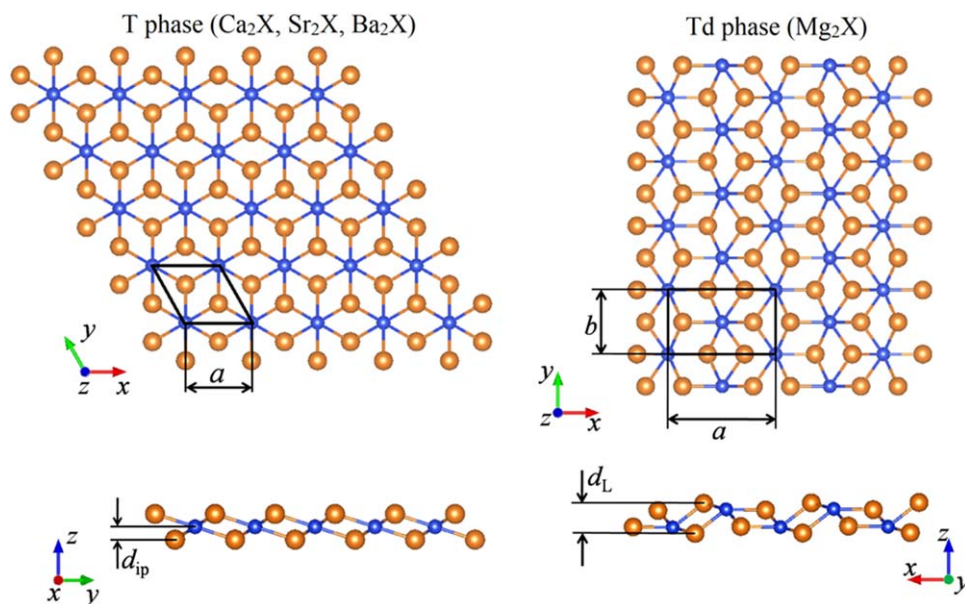
Fig. 1. (Color online) The top (the top panel) and lateral (the bottom panel) views of 2D Me$_2$X. The unit cell parameters (a) and (b), interplane distance (d_{ip}), thickness of the 2D structure (d_L) and crystallographic axes are shown. The larger spheres correspond to the Me atoms and the smaller spheres stand for the X atoms.

Table I.   The calculated structural parameters (a, $d_{Me–X}$, d_{ip}) of 2D Me$_2$X in the T-phase.

	Ca$_2$Si	Sr$_2$Si	Ba$_2$Si	Ca$_2$Ge	Sr$_2$Ge	Ba$_2$Ge	Ca$_2$Sn	Sr$_2$Sn	Ba$_2$Sn
a, Å	4.72	4.93	5.10	4.75	4.96	5.12	5.07	5.28	5.44
$d_{Me–X}$, Å	2.96	3.13	3.31	2.98	3.15	3.32	3.15	3.32	3.48
d_{ip}, Å	1.15	1.31	1.50	1.16	1.32	1.51	1.15	1.31	1.51

the harmonic approximation. The suggested reasons were proven by the results of some ab initio and molecular dynamics calculations where the phonon dispersions of different 2D materials were investigated.[38–43]

In this work the phonon dispersions of 2D Me$_2$X with different supercell sizes increased up to $7 \times 7 \times 1$ have been calculated. As an example in Fig. 2 we show the corresponding changes in the phonon dispersion of 2D Sr$_2$Ge. It is clear that the region of imaginary frequencies near the Γ point disappears with the supercell size. In fact, at the $5 \times 5 \times 1$ and larger supercell sizes the imaginary frequencies can not be spotted. The similar behavior we have observed for the other 2D Me$_2$X and Fig. 3 shows phonon spectra for all 2D Me$_2$X in the T phase without the imaginary frequencies. It also should be noted, that the presence of these imaginary frequencies in the ZA phonon branch in the vicinity of the Γ point does not affect the important values which can be extracted from phonons dispersions (i.e. the Debye and Einstein temperatures, the frequencies of optical active phonon modes, the sound speed). The knowledge of these values is very crucial when, for example, performing modeling of charge carrier mobility versus temperature behavior in semiconducting materials such as BaSi$_2$.[44]

The Debye and Einstein temperatures of 2D Me$_2$X that denote the top of acoustic branches and the top of all phonon modes, respectively, as well as the properties of optical phonon modes in the Γ point and the sound speed are summarized in Tables II and III. The phonon dispersions of the considered 2D Me$_2$X in the T phase contain six optical phonon branches. In particular, there are three infrared active modes (A_{2u}, $2E_u$) and three Raman active modes (A_{1g}, $2E_g$) in

the Γ point. Since the Raman spectroscopy is a widely used, quick, convenient, nondestructive and noninvasive tool for the surface characterization of 2D structures at ambient conditions and without complicated sample preparation,[45] the calculated frequencies of optical active modes (see Table III) will be useful for the identification of the considered 2D Me$_2$X.

4.   Structure and phonon properties of 2D Mg$_2$X in the Td phase

The investigation of phonon dispersions in all 2D Me$_2$X revealed that 2D Mg$_2$X displayed imaginary frequencies at the Brillouin zone border contrary to 2D Ca$_2$X, Sr$_2$X and Ba$_2$X.[37] In this case neither the increase in the size of the unit cell (see Sect. 3 for 2D Sr$_2$Ge), nor going beyond the harmonic approximation can help to get rid of these imaginary frequencies indicating the dynamical instability of the T phase for 2D Mg$_2$X.[37] In addition, in Ref. 37 it was suggested that a slight orthorhombic distortion could transform the T phase into the Td phase (see Fig. 1) similar to some transition metal dichalcogenides[46–48] and all 2D Mg$_2$X could be viewed stable against the phonon excitation. These 2D Mg$_2$X in the Td phase also possessed lower total energies with respect to those of the corresponding 2D Mg$_2$X in the T phase (by 0.02, 0.03, and 0.10 eV per formula unit, respectively for 2D Mg$_2$Si, Mg$_2$Ge, and Mg$_2$Sn).[37] Even though some imaginary frequencies were present in the vicinity of the Γ point for 2D Mg$_2$Si and Mg$_2$Sn, 2D Mg$_2$Ge did not display imaginary frequencies in its phonon spectrum.[37] Our attempt to increase the supercell size of 2D Mg$_2$Si and Mg$_2$Sn up to $8 \times 5 \times 1$ did not lead to removing the
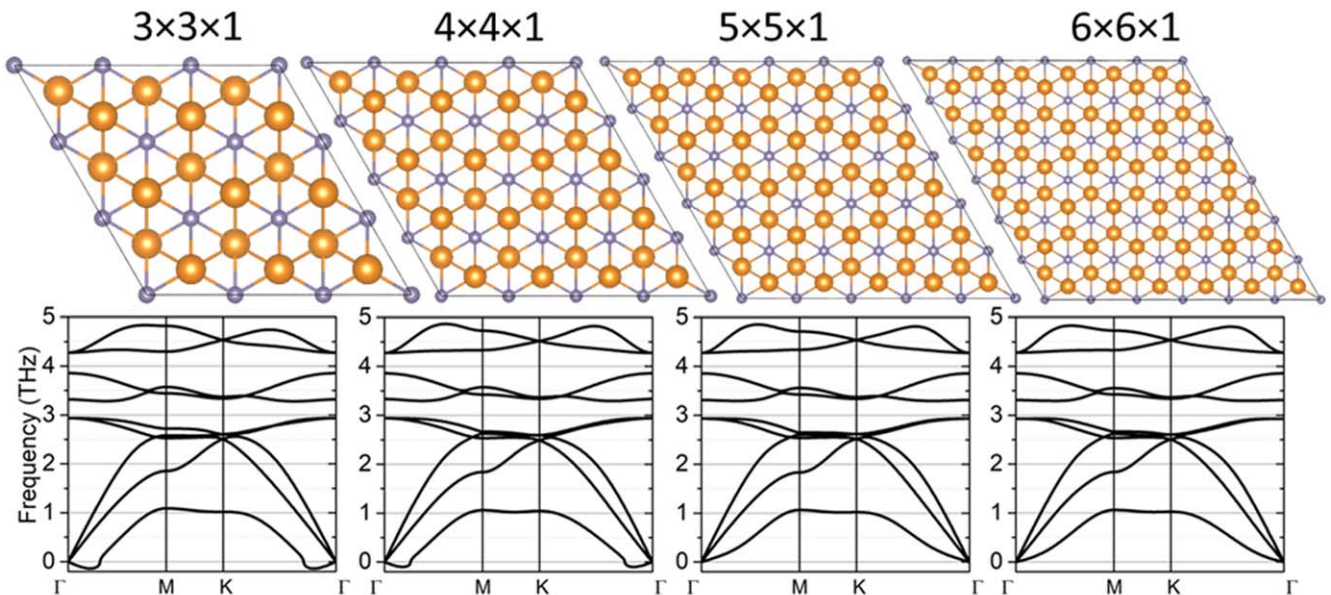
Fig. 2.   (Color online) The phonon dispersions (the bottom panel) of 2D Sr$_2$Ge with respect to the supercell size (the top panel). The larger spheres correspond to the Sr atoms and the smaller spheres correspond to the Ge atoms. The imaginary frequencies are indicated by negative values.
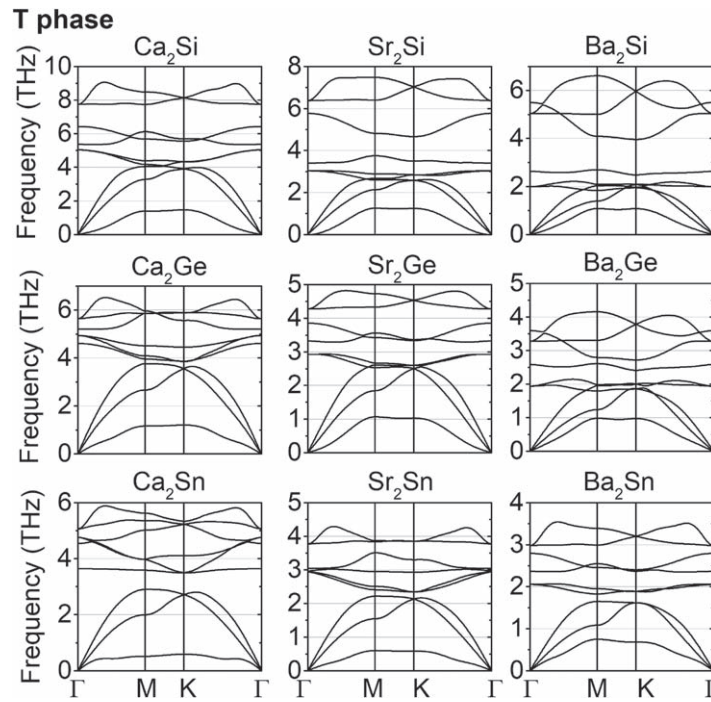
Fig. 3.   The phonon dispersions of 2D Me$_2$X in the T phase.

Table II.   The Debye and Einstein temperatures for 2D Me$_2$X in the T phase.

	Ca$_2$Si	Sr$_2$Si	Ba$_2$Si	Ca$_2$Ge	Sr$_2$Ge	Ba$_2$Ge	Ca$_2$Sn	Sr$_2$Sn	Ba$_2$Sn
T_D, K	193.0	126.2	100.3	180.7	123.9	92.6	138.9	106.4	79.1
T_E, K	435.5	358.8	317.4	313.0	231.5	199.5	282.6	205.9	169.9

Table III.   Properties of phonon modes in the Γ point of 2D Me$_2$X in the T phase. IR–infrared and R–Raman active modes; TA–transverse and LA–longitudinal acoustic branches.

	A_{2u}	A_{1g}	E_g	E_u		
		Optical activity			Sound speed, m s^{-1}	
	IR	R	R	IR		
		Vibrating atoms				
	Me + X	Me	Me	Me + X		
		Frequency, THz			TA	LA
Ca$_2$Si	6.42	5.36	5.04	7.75	3777	5870
Ca$_2$Ge	4.61	5.20	4.94	5.64	3661	5225
Ca$_2$Sn	3.57	4.62	4.75	5.04	2712	4238
Sr$_2$Si	5.76	3.39	3.02	6.38	2530	3956
Sr$_2$Ge	3.86	3.33	2.93	4.28	2018	3361
Sr$_2$Sn	2.97	3.05	2.94	3.77	2100	3320
Ba$_2$Si	5.50	2.63	1.99	5.04	1792	2842
Ba$_2$Ge	3.55	2.59	1.92	3.28	1521	2548
Ba$_2$Sn	2.79	2.36	2.06	2.98	1500	2499

imaginary frequencies probably indicating that the supercell size should be further increased.

The orthorhombic distortion of the T phase required doubling of the number of atoms in the unit cell as compared to the hexagonal one (see Fig. 1): two Mg atoms and four X atoms. The unit cell is shown in Fig. 1. Moreover, the perfect layered structure (two Mg surface layers and one X layer in between) is distorted since the X atoms shift closer to the surface (see the lateral view in Fig. 1). This structure can not be described by the interplane distances (d_ip) and we instead of this suggest using the thickness of the structure itself (d_L) as indicated in Fig. 1. In accordance with the trend of increasing the Me–X interatomic distances when Me is changed (see discussion in Sect. 3), the Mg–X interatomic distances are smaller than the corresponding Ca–X, Sr–X or Ba–X ones (compare data in Tables I and IV).

Since the appearance of the imaginary frequencies in the phonon spectra near the Γ point did not affect the Debye and Einstein temperatures as well as the other properties of 2D Me$_2$X, we could summarized their values in Tables V and VI. The phonon dispersions of 2D Mg$_2$X in the Td phase contain fifteen optical phonon branches. Six phonon modes in the Γ point are infrared active ($2A_u$, $4B_u$) and nine ones are Raman active ($6A_u$, $3B_u$). The frequencies of all phonon modes in the Γ point, the Debye and Einstein temperatures, and the sound speeds decrease in the row Mg$_2$Si–Mg$_2$Ge–Mg$_2$Sn in accordance with the increase of atom masses and all the values are smaller than the corresponding values for 2D Ca$_2$X in the T phase.

Table IV.   The calculated structural parameters (a, b, $d_\mathrm{Mg–X}$, $d_\mathrm{X–X}$, d_ML) of 2D Mg$_2$X in the Td-phase.

	Mg$_2$Si	Mg$_2$Ge	Mg$_2$Sn
a, Å	7.28	7.31	7.40
b, Å	4.34	4.37	4.66
$d_\mathrm{Mg–X}$, Å	2.65–2.68	2.68–2.70	2.88–2.91
$d_\mathrm{X–X}$, Å	4.34–4.43	4.37–4.47	4.66–4.88
d_L, Å	2.03	2.07	2.26

Table V. The Debye and Einstein temperatures for 2D Mg_2X in the Td phase.

	Mg_2Si	Mg_2Ge	Mg_2Sn
T_D, K	222.3	163.2	110.8
T_E, K	532.3	441.1	406.0

5. Electronic properties of 2D Me₂X

As we have indicated in our previous work, the charge distribution between atoms in 2D Me_2Si depended only on the electronegativity of the Me atoms.[19] In the case of 2D Me_2X the charge transfer from the Me atoms to X atoms, which is more than $1e^-$, follows the same trends: the electronegativity of the Me atoms defines the charge distribution (see Table VII). Such a pronounced charge transfer clearly indicates the ionic nature of the chemical bonding. This issue originates from the fact that the X–X interatomic distances are too large (see the corresponding a values in Table I and IV) while the Me–X bonds define the structure of 2D Me_2X. If the X atoms are the first neighbors to themselves, as in $BaSi_2$ bulk,[49] the covalent bonding gives an essential contribution to the overall bonding in this silicide.

The calculated electronic band structures of 2D Mg_2X in the Td phase and 2D Ca_2X, Sr_2X and Ba_2X in the T phase are shown in Fig. 4. It is evident that all considered 2D Me_2X are semiconductors and their band-gap values are summarized in Table VII. The dispersion of the highest in energy valence band of all 2D Mg_2X in the Td phase is almost identical and clearly indicates the presence of a well-resolved maximum in the Γ point. This maximum is mainly defined by the X-p states with a slight admixture of the Mg-p states. In the conduction band there are two distinct minima located in the Γ and $0.4 \times$ S–Y points, which are characterized by the X-p and X-s states in addition to the Mg-p and Mg-s states. For 2D Mg_2Si and Mg_2Ge the direct nature of the gap can be spotted, while 2D Mg_2Sn is an indirect band-gap semiconductor. In addition, for 2D Mg_2Sn the third local minimum in the lowest in energy conduction band is present in the vicinity of the Y point.

Contrary to 2D Me_2X in the Td phase, all 2D Me_2X in the T phase possess very small dispersion of the highest in energy valence band, which is in fact almost flat, with maxima in the M and K points due to the dominant contribution of the Me-d states. For 2D Ba_2X the local band maximum in the K point is shifted towards the Γ point. At variance with this, the lowest in energy conduction band has well-defined minimum in the Γ point where a sizable admixture of the X-s and X-p states to the Me-d states are identified. Strictly speaking, 2D Me_2X in the T phase are indirect band-gap semiconductors. However, due to a small energy difference (a few meV) between the main valence band maxima in the M, K points and in the Γ point, (the latter is a saddle point), 2D Ca_2X can be considered as quasidirect semiconductors. As we have indicated in our previous study,[19] the presence of the d states of the Ca, Sr and Ba atoms near the gap region and, as a result, the pronounced p–d hybridization with the p states of the X atoms could be the reason for the different dispersion of the bands located close to the gap as compared to that of the Mg based compounds, where the s–p hybridization occurred.

Since for the band structure calculations we used the hybrid potential, the calculated gap values could be expected to be close to the experimental ones. In fact, for some Me_2Si cubic bulks our band-gap estimates almost coincided with the available experimental data as well as with the results of quasiparticle calculations within the GW approximation (see discussion in Ref. 19). Thus, our predictions can be viewed as reliable also for 2D Me_2X. Thus, in the row of 2D Mg_2Si–Mg_2Ge–Mg_2Sn in the Td phase the band-gap sizably drops from 0.95 to 0.65 eV and then it stays almost unchanged −0.63 eV. On the contrary, for 2D Ca_2X, Sr_2X and Ba_2X in the T phase there are two clear trends: (1) when only X atoms are replaced, initially the gap slightly decreases from silicides to germanides with the following significant rise for stannides (for instance, 0.69–0.63–1.01 eV for 2D Ca_2Si–Ca_2Ge–Ca_2Sn); (2) if only Me atoms are replaced, the band-gap constantly decreases when moving from silicides to germanides and further to stannides (for instance 0.63–0.23–0.12 eV for 2D Ca_2Ge–Sr_2Ge–Ba_2Ge). The band-gap variations in rows of isostructural silicide bulk materials can be attributed to the different extent of the Me $3d$ or $4d$ or $5d$ orbitals and their overlap with the p-orbitals of the X atoms leading to different band dispersion near the gap region and, as a result, to variation in gap values. Similar issues have already been discussed for β-$FeSi_2$ and $OsSi_2$.[50] Quantum confinement effects can lead to an increase of the gap for a nanostructure with respect to that in the parent bulk material. In addition, surface effects can stabilize (or even decrease) the gap values since the valence band maximum and/or the conduction band minimum are defined by the surface states, which are not affected by quantum confinement effects. This is the case for 2D Me_2X in the T phase where the Me-d states dominate the gap region making it difficult to explain band-gap variations in the rows of studied 2D Me_2X. Discussion on a delicate balance between

Table VI. Properties of phonon modes at Γ point of 2D Mg_2X in the Td phase. IR–infrared and R–Raman active modes; TA–transverse and LA–longitudinal acoustic branches.

|	A_g	B_u	B_g	A_g	A_u	B_u	A_g	A_g	B_g	A_g	A_u	B_u	B_u	A_g	B_g	Sound speed, m s⁻¹	
	Irreducible representation Optical activity																
	R	IR	R	R	IR	IR	R	R	R	R	IR	IR	IR	R	R	TA	LA
	Frequency, THz																
Mg_2Si	2.51	4.40	4.57	5.06	5.70	6.22	6.33	7.05	7.70	7.82	9.41	9.53	9.59	9.92	10.10	4982	6543
Mg_2Ge	1.73	3.96	3.23	5.30	5.20	4.74	4.18	5.96	7.21	6.77	7.06	9.00	7.32	8.15	8.18	3510	4984
Mg_2Sn	1.72	2.99	2.21	4.04	4.60	4.21	3.23	4.97	6.39	6.04	5.71	8.39	6.34	7.70	7.09	2464	3551

Table VII. The calculated charge transfer (q_{Me}, q_X) and band gaps (E_g) of all 2D Me_2X.

	Mg$_2$Si	Mg$_2$Ge	Mg$_2$Sn	Ca$_2$Si	Ca$_2$Ge	Ca$_2$Sn	Sr$_2$Si	Sr$_2$Ge	Sr$_2$Sn	Ba$_2$Si	Ba$_2$Ge	Ba$_2$Sn
q_{Me}, e^-	1.47	1.44	1.37	1.39	1.37	1.38	1.27	1.26	1.29	1.12	1.11	1.15
q_X, e^-	2.94	2.88	2.74	2.78	2.74	2.76	2.54	2.52	2.58	2.24	2.22	2.30
E_g, eV	0.95	0.65	0.63	0.69	0.63	1.01	0.33	0.23	0.63	0.19	0.12	0.45
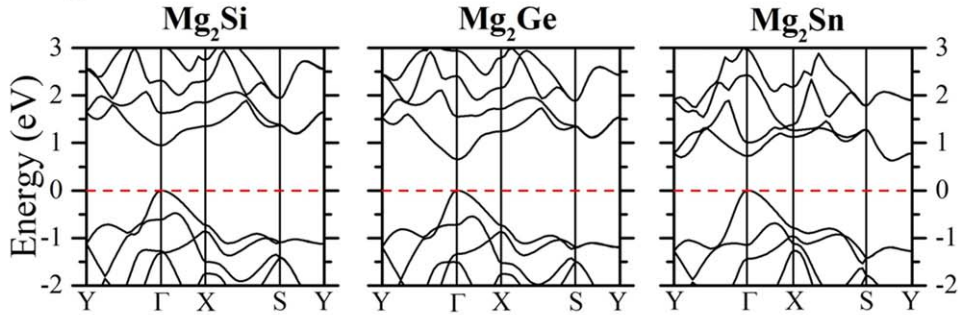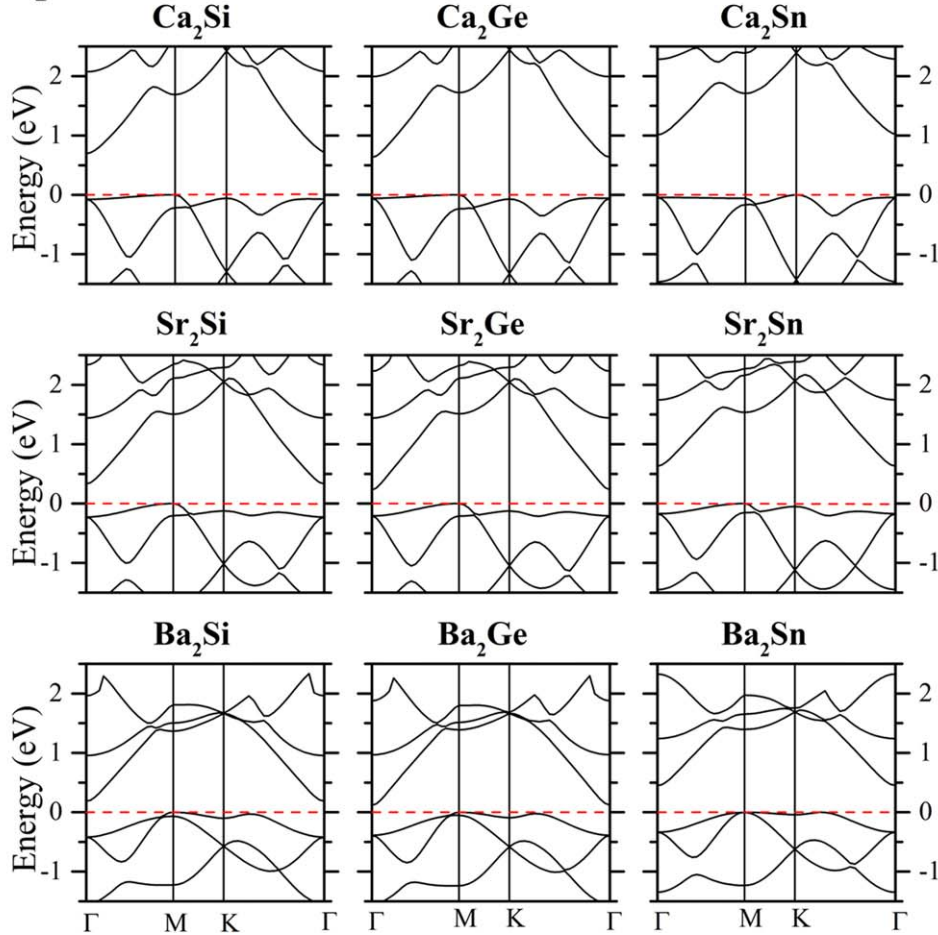
Fig. 4. (Color online) Band structures of 2D Me_2X in different phases. Zero at the energy scale corresponds to the top of the valence band.

quantum confinement and surface effects has been provided for thin films of BaSi$_2$[35] and different nanostructures of TiO$_2$.[51,52]

One more issue here should be clarified in detail concerning the pseudo passivation effect. When one deals with surface dangling bonds it is very important to know about the nature of the chemical bonding of a compound under investigation. If it is a covalent nature (like in silicon or germanium), hydrogen is often used to saturate dangling bonds, which are directional, in order to calculate an energy spectrum near the gap region since surface states associated with dangling bonds "feel" the gap region indicating metallic-like properties.[53] Hydrogen saturation of dangling bonds "cleans up" the gap by moving occupied stated down in energy and unoccupied states up in energy providing semiconductor-like properties.[54,55] In the case of an ionic nature, hydrogen is not necessary for the dangling bond passivation because a dangling bond is not directional and a

charge transfer can effectively "eliminate" this dangling band. Usually, the energy spectrum of a slab of an ionic compound does not contain localized bands associated with dangling bonds, while enforced hydrogen surface "passivation" can lead to the appearance of such bands as observed in Ref. 51 for TiO_2 nanostructures.

Direct band-gap semiconducting nanostructures can be promising for various optoelectronic applications especially if their first direct transition possesses the high oscillator strength. The squared dipole matrix element is the key ingredient to estimate the oscillator strength of an energy transition. In Table VIII we summarized the normalized values of the squared dipole matrix elements for the first direct transition in the Γ point of direct band-gap 2D Mg_2X with respect to the one of the GaAs bulk (M^2_{2D}/M^2_{GaAs}). For the sake of comparison the similar analysis has been performed for quasidirect 2D Ca_2X. For nanostructures it is very important to take into account the so-called depolarization or local-field effects which sizably attenuate absorption at lower energies when the polarization of the light is perpendicular to a nanostructure surface.[56] Since this procedure is extremely computationally expensive and it has not been utilized in our study, we would like to point out that any component of M for the $\mathbf{E}_\perp$ light polarization should be considered to be sizably smaller, while for the $\mathbf{E}_\parallel$ light polarization our predictions can be reasonable. It is evident that only 2D Ca_2X can efficiently absorb (and probably emit) light.

6. Structure and electronic properties of ternary 2D Me_2X

The formation of ternary compounds on the basis of isostructural binary compounds is a feasible way to modify the electronic and optical properties of materials.[57] As we have indicated in Sects. 3–5, only changes in the Me atoms provided sizable variations in interatomic and interplane distances and in the charge transfer between the atoms in 2D Me_2X (see Tables I, IV and VII). Thus, it is reasonable to construct ternary 2D Me_2X as 2D MeMe′X where one surface layer consists of the Me atoms and another one—of the Me′ atoms, making for example 2D MgCaSi as shown in Fig. 5. In this case the interatomic and iterplane distances will be unavoidably altered with respect to those in the parent 2D structures. Therefore, it is quite possible to expect changes not only in the charge transfer but also in the electronic and optical properties.

Table VIII. The calculated values of the squared dipole matrix elements for the first direct transition in the Γ point for some 2D Me_2X with respect to the one of the GaAs bulk (M^2_{2D}/M^2_{GaAs}).

Td phase	Mg₂Si	Mg₂Ge	Mg₂Sn
$\mathbf{E}_\parallel$	0	0	0
$\mathbf{E}_\perp$	0.25	0.46	0.29

T phase	Ca₂Si	Ca₂Ge	Ca₂Sn
$\mathbf{E}_\parallel$	0.10	0.15	0.16
$\mathbf{E}_\perp$	0	0	0
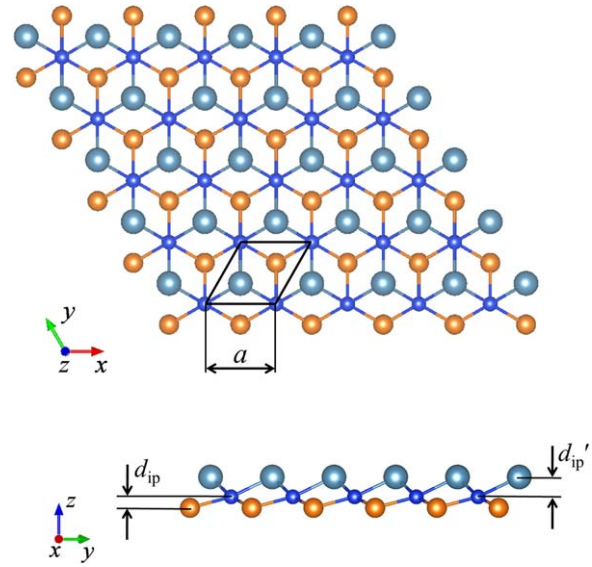
Fig. 5. (Color online) The top (the top panel) and lateral (the bottom panel) views of 2D MeMe′X in the T phase. The interplane distances (d_{ip}, d_{ip}') are shown. The largest, medium and smaller size spheres correspond to the Me′, Me and X atoms, respectively.

We have found that none of 2D MeMe′X can be stabilized in the Td phase even for Mg-based ternary 2D compounds after the full structural optimization which indicated only the T phase. Thus, the T phase can be viewed as a ground state for all 2D MeMe′X. The investigation of phonon properties revealed a small region of imaginary frequencies in the phonon spectra near the Γ point of 2D MeMe′X even for the $7 \times 7 \times 1$ supercells. Since such imaginary frequencies do not affect the Debye and Einstein temperatures of 2D MeMe′X, they are listed in Tables IX–XI. These temperatures, as well as phonon

Table IX. The calculated structural parameters (a, $d_{Me–Si}$, $d_{Me′–Si}$, d_{ip}, d_{ip}'), charge transfer (q_{Me}, $q_{Me′}$, q_{Si}), Debye and Einstein temperatures (T_D, T_E), and band gaps (E_g) of 2D MeMe′Si.

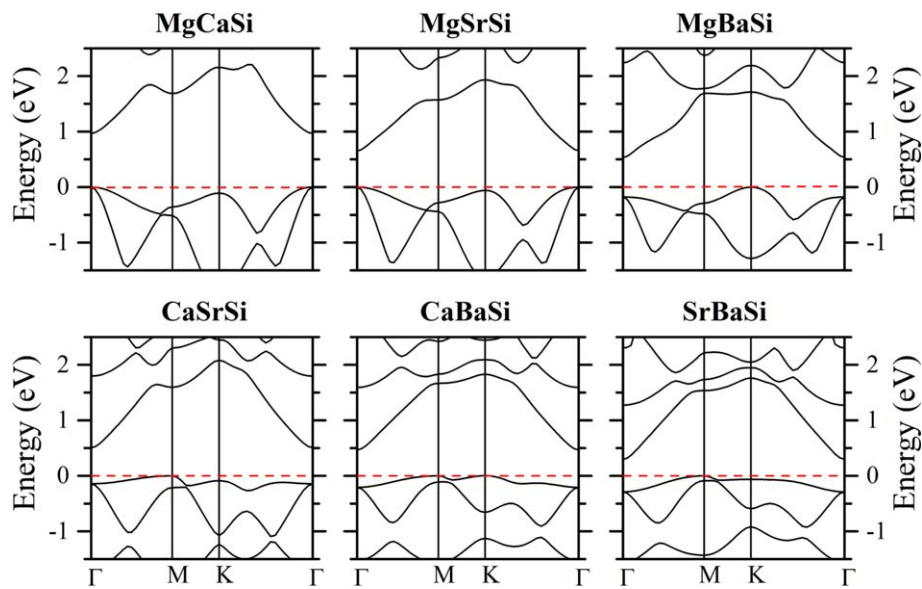|	MgCaSi	MgSrSi	MgBaSi	CaSrSi	CaBaSi	SrBaSi
a, Å	4.52	4.59	4.67	4.82	4.89	5.00
$d_{Me–Si}$, Å	2.70	2.73	2.77	2.99	3.02	3.16
$d_{Me′–Si}$, Å	2.90	3.04	3.17	3.10	3.24	3.27
d_{ip}, Å	0.68	0.63	0.62	1.09	1.07	1.28
d_{ip}', Å	1.26	1.48	1.66	1.37	1.59	1.53
q_{Me}, e^-	1.43	1.41	1.39	1.39	1.39	1.29
$q_{Me′}$, e^-	1.39	1.25	1.05	1.26	1.07	1.09
q_{Si}, e^-	2.82	2.66	2.44	2.65	2.46	2.38
T_D, K	198.2	142.1	118.5	138.2	113.7	107.0
T_E, K	479.9	440.1	414.7	393.5	373.4	349.9
E_g, eV	0.97	0.65	0.53	0.51	0.47	0.30

Fig. 6. (Color online) Band structures of 2D MeMe′Si. Zero at the energy scale corresponds to the top of the valence band.
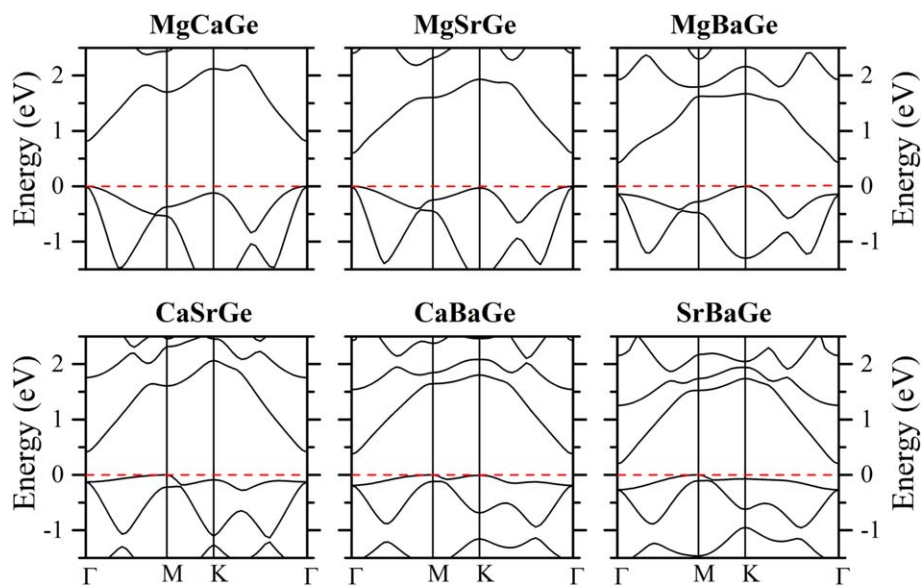
Fig. 7. (Color online) Band structures of 2D MeMe′Ge. Zero at the energy scale corresponds to the top of the valence band.
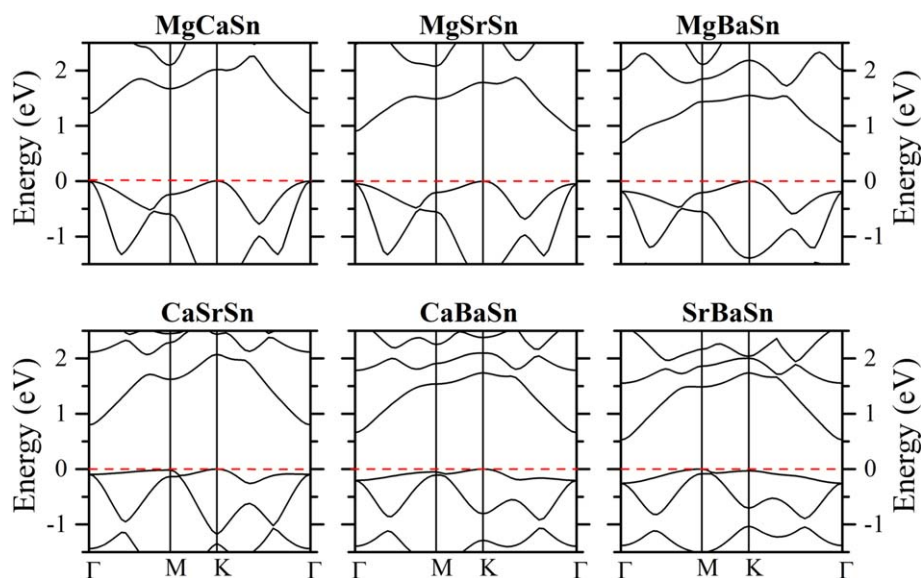
Fig. 8. (Color online) Band structures of 2D MeMe′Sn. Zero at the energy scale corresponds to the top of the valence band.

Table X.   The calculated structural parameters (a, $d_{\text{Me–Ge}}$, $d_{\text{Me'–Ge}}$, d_{ip}, d_{ip}'), charge transfer (q_{Me}, $q_{\text{Me'}}$, q_{Ge}), Debye and Einstein temperatures (T_{D}, T_{E}), and band gaps (E_{g}) of 2D MeMe'Ge.

	MgCaGe	MgSrGe	MgBaGe	CaSrGe	CaBaGe	SrBaGe
a, Å	4.56	4.65	4.71	4.85	4.92	5.04
$d_{\text{Me–Ge}}$, Å	2.73	2.76	2.79	3.01	3.04	3.18
$d_{\text{Me'–Ge}}$, Å	2.92	3.06	3.20	3.12	3.26	3.29
d_{ip}, Å	0.70	0.64	0.64	1.10	1.08	1.29
d_{ip}', Å	1.25	1.47	1.68	1.38	1.60	1.54
q_{Me}, e^-	1.41	1.38	1.36	1.37	1.37	1.28
$q_{\text{Me'}}$, e^-	1.38	1.25	1.05	1.26	1.07	1.08
q_{Ge}, e^-	2.79	2.63	2.41	2.63	2.44	2.36
T_{D}, K	179.0	131.0	112.3	132.9	109.9	103.7
T_{E}, K	375.3	339.3	318.2	268.8	252.4	218.4
E_{g}, eV	0.81	0.59	0.42	0.41	0.38	0.20

Table XI.   The calculated structural parameters (a, $d_{\text{Me–Sn}}$, $d_{\text{Me'–Sn}}$, d_{ip}, d_{ip}'), charge transfer (q_{Me}, $q_{\text{Me'}}$, q_{Sn}), Debye and Einstein temperatures (T_{D}, T_{E}), and band gaps (E_{g}) of 2D MeMe'Sn.

	MgCaSn	MgSrSn	MgBaSn	CaSrSn	CaBaSn	SrBaSn
a, Å	4.87	4.95	5.02	5.17	5.24	5.36
$d_{\text{Me–Sn}}$, Å	2.89	2.91	2.95	3.17	3.20	3.34
$d_{\text{Me'–Sn}}$, Å	3.09	3.23	3.37	3.29	3.43	3.46
d_{ip}, Å	0.64	0.55	0.54	1.07	1.04	1.27
d_{ip}', Å	1.27	1.51	1.72	1.38	1.62	1.54
q_{Me}, e^-	1.36	1.33	1.30	1.37	1.37	1.29
$q_{\text{Me'}}$, e^-	1.38	1.29	1.11	1.29	1.13	1.14
q_{Sn}, e^-	2.72	2.62	2.41	2.66	2.50	2.23
T_{D}, K	142.5	111.3	97.4	113.7	95.0	91.7
T_{E}, K	363.3	332.6	311.0	243.8	229.4	182.4
E_{g}, eV	1.23	0.90	0.70	0.80	0.66	0.53

Table XII.   The calculated values of the squared dipole matrix elements for the first direct transition in the Γ point for some 2D MeMe'X with respect to the one of the GaAs bulk ($M^2_{\text{2D}}/M^2_{\text{GaAs}}$).

	MgCaSi	MgSrSi	MgCaGe	MgSrGe
$\mathbf{E}_{\parallel}$	0.15	0.14	0.23	0.51
$\mathbf{E}_{\perp}$	0	0	0	0

frequencies, have values in between of the corresponding values of parent 2D Me$_2$X.

The optimized lattice parameters, interatomic and interplane distances for 2D MeMe'X in the T phase are summarized in Tables IX–XI. One can indeed see some distortion with respect to the parent 2D Me$_2$X. For example, in the case of 2D CaSrSi, the corresponding values of a change from 4.72 Å (2D Ca$_2$Si) to 4.82 Å (2D CaSrSi) and to 4.93 Å (2D Sr$_2$Si), $d_{\text{Me–X}}$ varies from 2.96 Å (2D Ca$_2$Si) to 2.99 Å (for $d_{\text{Ca–Si}}$ in 2D CaSrSi) to 3.10 Å (for $d_{\text{Sr–Si}}$ in 2D CaSrSi) and to 3.13 Å (2D Sr$_2$Si), d_{ip} spans from 1.15 Å (2D Ca$_2$Si) to 1.09 Å (between the Ca and Si layers in 2D CaSrSi) to 1.37 Å (between the Sr and Si layers in 2D CaSrSi) and to 1.31 Å (2D Sr$_2$Si). These deviations are also evident in the lateral view of 2D MeMe'X in Fig. 5. Since the Me and Me' atoms donate almost the same amount of charge like in the parent 2D Me$_2$X, to balance the charge transfer in 2D ternary compounds the X atoms have to accept different charges as compared to the charges in the binary compounds. For instance, in the case of 2D CaSrSi the Ca and Sr atoms donate respectively 1.39 e^- and 1.26 e^- (1.39 e^- and 1.27 e^- in their parent 2D Me$_2$X) and the Si atoms accept 2.65 e^- to be compared with 2.78 e^- (2D Ca$_2$Si) and 2.54 e^- (2D Sr$_2$Si).

The calculated band structures for all 2D MeMe'X are presented in Figs. 6–8. It is evident that the considered 2D ternary compounds are semiconductors and their band gaps are summarized in Tables IX–XI. The dispersion of the lowest in energy conduction band is almost identical for all 2D MeMe'X displaying the minimum in the Γ point where the Me-s and X-s states are prevailing. Only 2D MgCaSi, MgSrSi, MgCaGe and MgSrGe are direct band-gap semiconductors because their maximum of the valence band is in the Γ point, which is due to the X-p, Me-p and Me-d states. There is another local maximum in the K point which is a few meV lower in energy. 2D MgBaX have the band valence maximum in the K point, where all the rest of 2D MeMe'X— in the M point. As parent 2D Me$_2$X in the T phase, all 2D MeMe'X have very small dispersion of the highest in energy valence band. The performed analysis of the character of the states in the band extrema in the Γ point for direct band-gap materials (2D MgCaSi, MgSrSi, MgCaGe and MgSrGe) indicates that the first direct transition is not closed in the dipole approximation. In fact, the corresponding $M^2_{\text{2D}}/M^2_{\text{GaAs}}$ ratios are rather high and comparable with 2D Me$_2$X (compare data in Tables VIII and XII). Eventually, band-gap variations in 2D MeMe'X follow the same trends for parent 2D Me$_2$X as we have already discussed in Sect. 5.

7. Conclusions

In this review paper we have presented our recent results of ab initio calculations with the hybrid functional on structural stability and electronic properties of 2D Me$_2$X (Me=Mg, Ca, Sr, Ba and X=Si, Ge, Sn). Owing to the pseudo passivation effect and mostly ionic nature of the chemical bonding, it is

shown that the dangling bonds can efficiently be "eliminated" by transferring charges between atoms in 2D Me_2X. The latter fact and the absence of the imaginary frequencies in the phonon spectra of these nanostructures evidence the stability of 2D Me_2X and expand the family of known 2D materials. The considered 2D Me_2X are found to be semiconductors with the band-gap ranging from 0.12 to 1.01 eV. All 2D Mg_2X in the Td phase are direct band-gap semiconductors, while 2D Ca_2X in the T phase display a tiny difference in energy (a few meV) between the first direct and indirect transitions. Our estimates of the dipole matrix elements for the first direct transitions have pointed out sizable values of oscillator strength quite comparable to the one of the GaAs bulk. Even though the depolarization effects are expected to suppress absorption for 2D Mg_2X, a suitable substrate, which is necessary to fabricate these 2D Me_2X, attenuates the influence of the depolarization effects indicating nice perspective of 2D Mg_2Si, Mg_2Ge, Mg_2Sn, Ca_2Si, Ca_2Ge and Ca_2Sn as efficient light emitting materials. In addition, further attenuation of the depolarization effects can be reached if a thickness of Me_2X films is increased. It is quite possible that thicker Me_2X films are technologically easier to grow (rather than the true 2D form), however their thickness should be small enough to prevent the phase transition to the corresponding bulk structures. The formation of ternary 2D $MeMe'X$ compounds can be considered as the next possible way to tine or modify properties of parent 2D Me_2X. Moreover, for 2D $MeMe'X$ stripes (a few nm in size) it is not excluded that bending can occur since the total energy minimization provides changes in interatomic and interplane distances. This issue can lead to a possible 2D–1D transformation resulting in a $MeMe'X$ nanotube formation that requires a further investigation.

Acknowledgments

1) M. Chhowalla, D. Jena, and H. Zhang, Nat. Rev. Mater. **1**, 16052 (2016).
2) W. Yang, X. Zhang, and Y. Xie, Nano Today **11**, 793 (2016).
3) H. Tian, J. Tice, R. Fei, V. Tran, X. Yan, L. Yang, and H. Wang, Nano Today **11**, 763 (2016).
4) J. Shen, Y. Zhu, H. Jiang, and C. Li, Nano Today **11**, 483 (2016).
5) A. Molle, C. Grazianetti, L. Tao, D. Taneja, M. H. Alam, and D. Akinwande, Chem. Soc. Rev. **47**, 6370 (2018).
6) T. Sun, G. Zhang, D. Xu, X. Lian, H. Li, W. Chen, and C. Su, Mater. Today Energy **12**, 215 (2019).
7) Y. Xi, J. Zhuang, W. Hao, and Y. Du, ChemElectroChem **6**, 2841 (2019).
8) S. Balendhran, S. Walia, H. Nili, S. Sriram, and M. Bhaskaran, Small **11**, 640 (2015).
9) A. J. Mannix, B. Kiraly, M. C. Hersam, and N. P. Guisinger, Nat. Rev. Chem. **1**, 0014 (2017).
10) M. Velicky and P. S. Toth, Appl. Mater. Today **8**, 68 (2017).
11) G. Li, Y.-Y. Zhang, H. Guo, L. Huang, H. Lu, X. Lin, Y.-L. Wang, S. Du, and H.-J. Gao, Chem. Soc. Rev. **47**, 6073 (2018).
12) C. Grazianetti, E. Cinquanta, and A. Molle, 2D Mater. **3**, 012001 (2016).
13) J. Zhao et al., Prog. Mater. Sci. **83**, 24 (2016).
14) A. Acun et al., J. Phys.: Condens. Matter **27**, 443002 (2015).
15) Z. Meng, J. Zhuang, X. Xu, W. Hao, S. X. Dou, and Y. Du, Adv. Mater. Interfaces **5**, 1800749 (2018).
16) P. Miró, M. Audiffred, and T. Heine, Chem. Soc. Rev. **43**, 6537 (2014).
17) V. E. Borisenko, *Semiconducting Silicildes* (Springer, Berlin, 2000).
18) Y.-C. Lin, Y. Chen, and Y. Huang, Nanoscale **4**, 1412 (2012).
19) D. B. Migas, V. O. Bogorodz, A. B. Filonov, V. E. Borisenko, and N. V. Skorodumova, Surf. Sci. **670**, 51 (2018).
20) G. Kresse and J. Hafner, Phys. Rev. B **47**, 558 (1993).
21) G. Kresse and J. Furthmller, Comput. Mater. Sci. **6**, 15 (1996).
22) G. Kresse and J. Furthmller, Phys. Rev. B **54**, 11169 (1996).
23) G. Kresse and D. Joubert, Phys. Rev. B **59**, 1758 (1999).
24) J. Paier, R. Hirschl, M. Marsman, and G. Kresse, J. Chem. Phys. **122**, 234102 (2005).
25) J. Heyd, G. E. Scuseria, and M. Ernzerhof, J. Chem. Phys. **118**, 8207 (2003).
26) J. Heyd, G. E. Scuseria, and M. Ernzerhof, J. Chem. Phys. **124**, 219906 (2006).
27) J. Heyd and G. E. Scuseria, J. Chem. Phys. **120**, 7274 (2004).
28) J. Heyd and G. E. Scuseria, J. Chem. Phys. **121**, 1187 (2004).
29) W. Tang, E. Sanville, and G. Henkelman, J. Phys.: Condens. Matter **21**, 084204 (2009).
30) J. P. Perdew, K. Burke, and M. Ernzerhof, Phys. Rev. Lett. **77**, 3865 (1996).
31) A. Togo and I. Tanaka, Scr. Mater. **108**, 1 (2015).
32) T. Sohier, M. Gibertini, M. Calandra, F. Mauri, and N. Marzari, Nano Lett. **17**, 3758 (2017).
33) P. Blaha, K. Schwarz, G. K. H. Madsen, D. Kvasnicka, and J. Luitz, *WIEN2k, An Augmented Plane Wave + Local Orbitals Program for Calculating Crystal Properties* (Karlheinz Schwarz, Tech. Universität Wien, Vienna, 2001).
34) F. Tran and P. Blaha, Phys. Rev. B **83**, 235118 (2011).
35) D. B. Migas, V. O. Bogorodz, A. V. Krivosheeva, V. L. Shaposhnikov, A. B. Filonov, and V. E. Borisenko, Jpn. J. Appl. Phys. **56**, 05DA03 (2017).
36) D. B. Migas, V. O. Bogorodz, A. B. Filonov, V. L. Shaposhnikov, V. E. Borisenko, and N. G. Galkin, Jpn. J. Appl. Phys. **54**, 07JA03 (2015).
37) A. Y. Alekseev, A. G. Chernykh, A. B. Filonov, D. B. Migas, and N. V. Skorodumova, Int. J. Nanosci. **18**, 1940013 (2019).
38) S. Cahangirov, M. Topsakal, E. Aktürk, H. Şahin, and S. Ciraci, Phys. Rev. Lett. **102**, 236804 (2009).
39) C. Ataca, H. Şahin, and S. Ciraci, J. Phys. Chem. C **116**, 8983 (2012).
40) S. H. Lin and J. L. Kuo, Phys. Chem. Chem. Phys. **16**, 20763 (2014).
41) X. Li, Y. Dai, M. Li, W. Wei, and B. Huang, J. Mater. Chem. A **3**, 24055 (2015).
42) J. He, X. Li, P. Lyu, and P. Nachtigall, Nanoscale **9**, 2246 (2017).
43) M. Mushtaq, Y. Zhou, and X. Xiang, RSC Adv. **7**, 22541 (2017).
44) T. Deng, T. Suemasu, D. A. Shohonov, I. S. Samusevich, A. B. Filonov, D. B. Migas, and V. E. Borisenko, Thin Solid Films **661**, 7 (2018).
45) A. Jorio, M. S. Dresselhaus, R. Saito, and G. Dresselhaus, *Raman Spectroscopy in Graphene Related Systems* (Wiley, New York, 2011).
46) M. Calandra, Phys. Rev. B **88**, 245428 (2013).
47) K. C. Santosh, C. Zhang, S. Hong, R. M. Wallace, and K. Cho, 2D Mater. **2**, 035019 (2015).
48) M. Kan, H. G. Nam, Y. H. Lee, and Q. Sun, Phys. Chem. Chem. Phys. **17**, 14866 (2015).
49) M. Imai, M. Kumar, and N. Umezawa, Scr. Mater. **172**, 43 (2019).
50) D. B. Migas, L. Miglio, W. Henrion, M. Rebien, F. Marabelli, B. A. Cook, V. L. Shaposhnikov, and V. E. Borisenko, Phys. Rev. B **64**, 075208 (2001).
51) D. B. Migas, A. B. Filonov, V. E. Borisenko, and N. V. Skorodumova, Phys. Chem. Chem. Phys. **16**, 9479 (2014).

52) D. B. Migas, A. B. Filonov, V. E. Borisenko, and N. V. Skorodumova, Phys. Chem. Chem. Phys. **16**, 9490 (2014).
53) R. Rurali, A. Poissier, and N. Lorente, Phys. Rev. B **74**, 165324 (2006).
54) D. B. Migas, J. Appl. Phys. **98**, 054310 (2005).
55) D. B. Migas and V. E. Borisenko, Phys. Rev. B **76**, 035440 (2007).
56) F. Bruneval, S. Botti, and L. Reining, Phys. Rev. Lett. **94**, 219701 (2005).
57) D. B. Migas and L. Miglio, Appl. Phys. Lett. **79**, 2175 (2001).